Monthly Notices of the ROYAL ASTRONOMICAL SOCIETY

MNRAS **528,** 1930–1944 (2024) https://doi.org/10.1093/mnras/stae072
Advance Access publication 2024 January 12

Simultaneous multicolour transit photometry of hot Jupiters HAT-P-19b, HAT-P-51b, HAT-P-55b, and HAT-P-65b

H. Kang,[1,2] G. Chen,[1,3★] E. Pallé,[4,5] F. Murgas,[4,5] N. Abreu García,[4,5] J. de Leon,[6] G. Enoc,[4,5] E. Esparza-Borges,[4,5] I. Fukuda,[6] A. Fukui,[7,4] D. Galán,[4,5] Y. Hayashi,[6] K. Isogai,[8,6] T. Kagetani,[6] K. Kawauchi,[9,6] J. Korth,[10] J. H. Livingston,[11,12,13] R. Luque,[14] Y. Ma,[1] A. Madrigal-Aguado,[4] P. Meni,[4,5] P. Montañes Rodriguez,[15,4] M. Mori,[6] S. Muñoz Torres,[4] N. Narita,[7,11,4] J. Orell-Miquel,[4,5] H. Parviainen,[5,4] A. Peláez-Torres,[4,5] M. Stangret,[16] M. Tamura[17,11,12] and N. Watanabe[6]

Affiliations are listed at the end of the paper

Accepted 2024 January 5. in original form 2023 December 4

ABSTRACT

Accurate physical parameters of exoplanet systems are essential for further exploration of planetary internal structure, atmospheres, and formation history. We aim to use simultaneous multicolour transit photometry to improve the estimation of transit parameters, to search for transit timing variations (TTVs), and to establish which of our targets should be prioritized for follow-up transmission spectroscopy. We performed time series photometric observations of 12 transits for the hot Jupiters HAT-P-19b, HAT-P-51b, HAT-P-55b, and HAT-P-65b using the simultaneous four-colour camera MuSCAT2 on the Telescopio Carlos Sánchez. We collected 56 additional transit light curves from TESS photometry. To derive transit parameters, we modelled the MuSCAT2 light curves with Gaussian processes to account for correlated noise. To derive physical parameters, we performed EXOFASTv2 global fits to the available transit and radial velocity data sets, together with the *Gaia* DR3 parallax, isochrones, and spectral energy distributions. To assess the potential for atmospheric characterization, we compared the multicolour transit depths with a flat line and a clear atmosphere model. We consistently refined the transit and physical parameters. We improved the orbital period and ephemeris estimates, and found no evidence for TTVs or orbital decay. The MuSCAT2 broad-band transmission spectra of HAT-P-19b and HAT-P-65b are consistent with previously published low-resolution transmission spectra. We also found that, except for HAT-P-65b, the assumption of a planetary atmosphere can improve the fit to the MuSCAT2 data. In particular, we identified HAT-P-55b as a priority target among these four planets for further atmospheric studies using transmission spectroscopy.

Key words: techniques: photometric – planets and satellites: fundamental parameters – planets and satellites: individual: (HAT-P-19b, HAT-P-51b, HAT-P-55b, HAT-P-65b) – planetary systems.

1 INTRODUCTION

Since the discovery of the first exoplanet around a Sun-like star (Mayor & Queloz 1995), more than 5500 exoplanets have been found, three-quarters of them by transit. When an exoplanet transits its host star, part of the starlight is blocked by the planets in the line of sight of the observer, and the starlight passes through the day-night terminator of the exoplanet's atmosphere. With the flux variation of the planetary system, the transit parameters of the system can be calculated from the transit light curves, which carry information about the internal structure and formation process of the exoplanets (Seager & Mallén-Ornelas 2003; Fortney, Marley & Barnes 2007; Mordasini et al. 2016). Because the atmospheric opacity varies in different passbands, the properties of the planetary atmosphere can be studied through transmission spectra (Seager & Sasselov 2000; Charbonneau et al. 2002), potentially linking the atmospheric chemistry to the planet's formation history and habitability (Madhusudhan, Amin & Kennedy 2014; Madhusudhan et al. 2016; Mordasini et al. 2016).

Meaningful investigations of planetary internal structure, atmospheric properties, atmospheric evolution, formation, and migration histories all require precise determination of orbital and physical parameters for the planetary systems as input. In particular, precise transit parameters, together with the latest parallaxes provided by *Gaia* and additional constraints from spectral energy distributions and stellar evolution models, can improve the estimates of the physical parameters. In the past decade, simultaneous multi-channel imagers, such as GROND (Greiner et al. 2008) and MuSCAT1/2/3 (Narita et al. 2015, 2019, 2020), have been extensively used to conduct multicolour follow-up transit photometry. The simultaneous multicolour capability not only allows precise measurements of colour-independent transit parameters to revise physical parameters and to search for transit timing vari-

★ E-mail: guochen@pmo.ac.cn

ations (TTVs), but also helps validate candidate planets orbiting faint stars, constrain star-spot properties and stellar obliquity, and provide a preliminary assessment of planetary atmospheres (e.g. Chen et al. 2014; Mancini et al. 2014; Parviainen et al. 2019).

To refine orbital and physical parameters for the known hot Jupiter systems and to prioritize targets for future spectroscopic atmospheric characterization, we initiated a multicolour transit photometry observing campaign using the four-colour simultaneous camera MuSCAT2 (Narita et al. 2019) in the g, r, i, and z_s bands. In previous studies, we have found evidence for scattering features in the atmospheres of the hot Jupiters WASP-74b (Luque et al. 2020) and WASP-104b (Chen et al. 2021a) by combining the MuSCAT2 photometric measurements with those from transit spectrophotometry. Here, we present the MuSCAT2 transit observations for four Saturn-mass hot Jupiters, HAT-P-19b, HAT-P-51b, HAT-P-55b, and HAT-P-65b, complemented by archival data from the Transiting Exoplanet Survey Satellite (TESS).

HAT-P-19b is a Saturn-mass planet discovered by Hartman et al. (2011), with a mass of 0.29 M_J, a radius of 1.13 R_J, and an equilibrium temperature of 1010 K, orbiting a $V = 12.9$ mag star (0.84 $\mathrm{M}_\odot$, 0.82 $\mathrm{R}_\odot$, $T_\mathrm{eff} = 4990$ K, and [Fe/H] = 0.23) every 4.009 d. Follow-up transit photometry found no evidence for TTVs (Seeliger et al. 2015; Maciejewski et al. 2018; Baştürk et al. 2020; Hagey, Edwards & Boley 2022), except for Hagey, Edwards & Boley (2022)'s recent study suggesting an orbital decay rate of -57.7 ± 7.3 ms yr^{-1}. The atmosphere of HAT-P-19b has been studied by Mallonn et al. (2015), who observed one transit with OSIRIS at the Gran Telescopio Canarias (GTC) and derived a flat featureless transmission spectrum.

HAT-P-51b was discovered by Hartman et al. (2015). It is also a Saturn-mass planet, with a mass of 0.31 M_J, a radius of 1.29 R_J, and an equilibrium temperature of 1192 K, orbiting a $V = 13.4$ mag star (0.98 $\mathrm{M}_\odot$, 1.04 $\mathrm{R}_\odot$, $T_\mathrm{eff} = 5449$ K, and [Fe/H] = 0.27) every 4.218 d.

HAT-P-55b was discovered by Juncher et al. (2015), with a mass of 0.58 M_J, a radius of 1.18 R_J, and an equilibrium temperature of 1313 K, orbiting a $V = 13.2$ mag star (1.01 $\mathrm{M}_\odot$, 1.01 $\mathrm{R}_\odot$, $T_\mathrm{eff} =$ 5808 K, and [Fe/H] = −0.03) every 3.585 d.

HAT-P-65b was discovered by Hartman et al. (2016), with a mass of 0.53 M_J, a radius of 1.89 R_J, and an equilibrium temperature of 1930 K, orbiting a $V = 13.1$ mag star (1.21 $\mathrm{M}_\odot$, 1.86 $\mathrm{R}_\odot$, $T_\mathrm{eff} =$ 5835 K, and [Fe/H] = 0.10) every 2.605 d. Based on two transits with OSIRIS at the GTC, Chen et al. (2021b) reported the detection of TiO and possible evidence for Na and VO in the atmosphere of HAT-P-65b.

This paper is organised as follows. In Section 2, we summarize the transit observations and data reduction procedures. In Section 3, we describe the light-curve analysis for MuSCAT2 and TESS, and present the derived transit parameters and orbital period. In Section 4, we perform the global modelling to refine the physical parameters of the planetary systems. In Section 5, we discuss the wavelength dependence of the transit depth for future atmospheric characterization. Finally, we draw conclusions in Section 6.

2 OBSERVATIONS AND DATA REDUCTION

2.1 TCS/MuSCAT2 photometry

We observed 3 transits of HAT-P-19b, 3 transits of HAT-P-51b, 4 transits of HAT-P-55b, and 2 transits of HAT-P-65b using the four-colour imager MuSCAT2 (Narita et al. 2019) installed on the 1.52 m Telescopio Carlos Sánchez (TCS) in the Teide Observatory, Tenerife, Spain. MuSCAT2 has the ability to simultaneously observe in four broad passbands: g (400–550 nm), r (550–700 nm), i (700–820 nm), and z_s (820–920 nm). Each passband has its independent CCD and each CCD has 1024 × 1024 pixels, with a pixel scale of ∼0.44 arcsec, giving MuSCAT2 a field of view of 7.4 × 7.4 arcmin^2. Due to CCD failure, only three channels were available in some nights. The detailed observation information is given in Table 1.

We reduced the MuSCAT2 data with customised IDL scripts as detailed in Chen et al. (2021a). In brief, we corrected bias, dark and flat field from the raw images, and performed aperture photometry using the APER routine from DAOPHOT.[1] We extracted the central time of each exposure and converted it to Barycentric Julian Dates in Barycentric Dynamical Time ($\mathrm{BJD_{TDB}}$; Eastman, Siverd & Gaudi 2010). We determined the best aperture radius by minimizing the light-curve scatter among a grid of radii ranging from 3 to 32 pixels (equivalent to 1.3–14.1 arcsec). We also tested different combinations of reference stars to produce the best synthetic reference light curve that minimizes the light-curve scatter. The final chosen aperture radii are listed in Table 1.

2.2 TESS photometry

To enlarge the mid-transit time data set for the refinement of the orbital period and ephemeris, we made use of the archival transit observations conducted by the TESS (Ricker et al. 2015).

– For HAT-P-19b, six transits with an exposure time of 1800 s were observed in full-frame images in Sector 17 between 2019 October 8 and November 2. Another seven transits with an exposure time of 20 s were observed in target pixel files in Sector 57 between 2022 September 30 and October 29.

– For HAT-P-51b, six transits with an exposure time of 1800 s were observed in full-frame images in Sector 17 between 2019 October 8 and November 2. Another six transits with an exposure time of 120 s were observed in full-frame images in Sector 57 between 2022 September 30 and October 29.

– For HAT-P-55b, thirteen transits with an exposure time of 120 s were observed in target pixel files in Sector 25 and 26 between 2020 May 14 and July 4. Another thirteen transits with an exposure time of 120 s were observed in target pixel files in Sectors 52 and 53 between 2022 May 25 and July 8 of which two transits were not used in the subsequent analysis due to incomplete transit coverage.

– For HAT-P-65b, ten transits of HAT-P-65b with an exposure time of 120 s were observed in target pixel files in Sector 55 in 2022 August 5 and September 1, and three transits of HAT-P-65b were not used in the subsequent analysis due to bad data quality.

We used the PYTHON package LIGHTKURVE (Lightkurve Collaboration 2018) to download the observation data from the MAST data archive.[2] For HAT-P-19b and HAT-P-51b, the raw light curves in 2019 were created from the tesscut product from full-frame images, and the SPOC light curves (Jenkins et al. 2016) were used in 2022. For HAT-P-55b, all the raw light curves were created from the target pixel file from tess phot. For HAT-P-65b, the SPOC light curves were used. The adopted time windows were three times the transit duration from the expected transit centre for data with an exposure time of 1800 s, one and a half times for data with 120 s, and one times for data with 20 s. The raw light curves were

[1] https://idlastro.gsfc.nasa.gov/ftp/pro/idlphot/
[2] https://archive.stsci.edu/

Table 1. Observation summary.

#	Tele.	Instru.	Start night UT	Start UT	End UT	Filter	t_{exp} (s)	Airmass[a]	Aperture (pixel)
HAT-P−19									
1	TCS	MuSCAT2	2018-07-23	01:02	05:21	g, r, i, z_s	25, 25, 15, 25	1.920–1.009-1.009	10, 11, 11, 10
2	TCS	MuSCAT2	2018-08-04	00:16	05:33	g, r, i, z_s	25, 15, 15, 25	1.904–1.007-1.018	7, 8, 7, 7
3	TCS	MuSCAT2	2018-08-08	01:01	05:41	g, r, i, z_s	10, 6, 10, 15	1.444–1.007-1.034	13, 14, 11, 11
HAT-P−51									
1	TCS	MuSCAT2	2018-10-16	22:46	05:19	g, r, i, z_s	60,60,15,60	1.119–1.003-1.854	15, 12, 11, 11
2	TCS	MuSCAT2	2018-11-23	23:17	03:08	g, r, i	30,15,30	1.020–1.020-1.888	10, 10, 10
3	TCS	MuSCAT2	2019-08-04	01:04	05:32	g, r, i	30,15,30	1.918–1.004-1.004	11, 10, 11
HAT-P−55									
1	TCS	MuSCAT2	2018-05-15	23:21	04:04	g, r, i, z_s	40–70,20-40,30-60,50-70	1.558–1.001-1.025	12, 6, 9, 9
2	TCS	MuSCAT2	2019-06-17	21:32	02:54	r, i, z_s	15–18,35,60	1.444–1.001-1.108	9, 10, 11
3	TCS	MuSCAT2	2019-08-17	21:00	01:14	g, r, z_s	20,15,100	1.001–1.001-1.792	10, 9, 14
4	TCS	MuSCAT2	2021-06-21	22:46	05:05	g, r, i, z_s	45,15-30,60,60	1.111–1.001-1.880	10, 8, 12, 10
HAT-P−65									
1	TCS	MuSCAT2	2018-07-29	22:03	04:49	g, r, i, z_s	30, 30, 30, 40	1.654–1.041-1.468	11, 11, 11, 11
2	TCS	MuSCAT2	2019-08-16	21:05	01:05	g, r, z_s	40, 20, 120	1.562–1.041-1.053	11, 11, 11

[a]The first and third values refer to the airmass at the beginning and end of the observation. The second value gives the minimum airmass.

normalized by the decile value of the whole TESS raw flux of all transits.

3 LIGHT-CURVE ANALYSIS

We modelled the raw light curves with the transit model from Mandel & Agol (2002) using the PYTHON package BATMAN (Kreidberg 2015):

$$\mu(t;\theta) = m(t; R_p/R_\star, T_{\rm mid}, i, a/R_\star, u_1, u_2). \tag{1}$$

The free parameters of the transit model consist of radius ratio $R_p/R_\star$, mid-transit time $T_{\rm mid}$, orbital inclination i, orbital semimajor axis in units of the stellar radius $a/R_\star$, the quadratic limb-darkening coefficients (LDCs) u_1 and u_2. Circular orbits are adopted for HAT-P-51, HAT-P-55, and HAT-P-65. For HAT-P-19, the orbital eccentricity and argument of periastron were fixed to 0.084 and 256 deg (Hartman et al. 2011), respectively. The orbital period is fixed to literature values in the transit model. For the planetary systems which are diluted by an unresolved companion star, the transit model is revised to $\mu^*(t; \theta, f_c)$ to account for the flux dilution from the companion:

$$\mu^*(t;\theta, f_c) = \frac{\mu(t;\theta) + f_c}{1 + f_c}, \tag{2}$$

where $\mu(t; \theta)$ is the transit model without the dilution effect, f_c is the companion-to-target flux ratio.

We employed Gaussian processes (GP) to account for the correlated noise present in the light curves, which was first introduced to transmission spectroscopy by Gibson et al. (2012). The one-dimensional GP regression was performed by the PYTHON package CELERITE (Foreman-Mackey et al. 2017), which accepts time series as the input vector. The GP mean function was described by the transit model multiplied by a linear polynomial baseline function $b(\varphi)$. The GP covariance matrix $\boldsymbol{K}$ was described by a combined kernel which consisted of an approximated 3/2-order Matern kernel for time-correlated red noise and a jitter kernel for underestimated white noise:

$$\kappa(\tau;\sigma_1, \rho, \sigma_2) = \sigma_1^2\left(1 + \frac{\sqrt{3}\tau}{\rho}\right)\exp\left(-\frac{\sqrt{3}\tau}{\rho}\right) + \sigma_2^2\delta, \tag{3}$$

where $\tau = |t_i - t_j|$ is the distance between two data points in time, ρ and σ_1^2 are the length and variance scales of systematic noise, σ_2^2 is the variance of underestimated white noise.

We performed the affine invariant Markov Chain Monte Carlo (MCMC) ensemble sampler using the PYTHON package EMCEE (Foreman-Mackey et al. 2013) to explore the posterior probability distributions of the free parameters. We adopted uniform priors for most of the transit parameters, polynomial coefficients for the baseline function, and log-uniform priors for the GP hyperparameters. We imposed normal priors on the LDCs u_1 and u_2 (see Table A1). We calculated LDCs from the ATLAS stellar atmosphere models by interpolating in the model grids using the stellar parameters (Espinoza & Jordán 2015). We ran two short chains for the burn-in phase and one long to ensure convergence chain for formal production.

3.1 MuSCAT2 light curves

For the MuSCAT2 light curves, we adopted the baseline function $b(\varphi)$ in the form of

$$b(\varphi) = c_0 + c_1 x + c_2 y + c_3 s, \tag{4}$$

where x and y are the coordinates of the target, s is the full width at half maximum of the target's point spread function. The mean function of GP was $\mu^*(t;\, \theta, f_c)b(\varphi)$ for HAT-P-65 and $\mu(t;\, \theta)b(\varphi)$ for the others. HAT-P-65 has a background star located at 3.6 arcsec in the west according to Hartman et al. (2016). The background star could not be spatially resolved by the defocused MuSCAT2 observations. Therefore, we estimated the companion-to-target flux ratios f_c within the MuSCAT2 passbands, which were 0.0086, 0.0094, 0.0098, 0.0101 for g, r, i, and z_s, respectively, based on the GTC OSIRIS measurements presented in Chen et al. (2021b).

We performed two runs of light-curve modelling for each target. In the first run, we aimed to derive the common transit parameters. We jointly fitted multicolour light curves on a nightly basis. Each night had the same values of i, $a/R_\star$, and $T_{\rm mid}$ for all light curves, and each light curve had independent values of $R_p/R_\star$, u_1, and u_2. The coefficients of the baseline function and the GP hyperparameters were always light-curve dependent. We reported the weighted mean of i, $a/R_\star$, and $R_p/R_\star$ of all nights as the final updated values in Table 2.

Table 2. Derived transit parameters and orbital ephemeris.

Planet	Source	$R_p/R_\star$	i (deg)	$a/R_\star$	P (d)	T_0(BJD$_{\rm TDB}$)
HAT-P−19b						
	This work	0.1346 ± 0.0004	89.52 ± 0.20	12.84 ± 0.06	$4.00878322^{+0.00000019}_{-0.00000019}$	$2456610.863945^{+0.000071}_{-0.000071}$
	Hartman et al. (2011)	0.1418 ± 0.0020	88.2 ± 0.4	12.24 ± 0.67	4.008778 ± 0.000006	$2455091.53417 \pm 0.00034^a$
	Seeliger et al. (2015)	0.1378 ± 0.0014	88.51 ± 0.22	12.36 ± 0.09	4.0087842 ± 0.0000007	$2455091.53500 \pm 0.00015$
	Mallonn et al. (2015)	0.1390 ± 0.0012	88.89 ± 0.32	12.37 ± 0.21	–	–
	Maciejewski et al. (2018)	–	–	–	$4.00878332 \pm 0.00000059$	$2455091.53501 \pm 0.00015$
	Baştürk et al. (2020)	–	$89.11^{+0.42}_{-0.29}$	$12.66^{+0.43}_{-0.20}$	$4.00878330 \pm 0.00000033$	$2456827.337856 \pm 0.000085$
	Ivshina & Winn (2022)	–	–	–	$4.00878403 \pm 0.00000049$	$2456935.57551 \pm 0.00012$
	Kokori et al. (2022)	–	–	–	4.0087842 ± 0.0000004	$2456899.49658 \pm 0.00010$
HAT-P−51b						
	This work	0.1253 ± 0.0006	89.28 ± 0.30	10.86 ± 0.08	$4.21802091^{+0.00000066}_{-0.00000066}$	$2458349.53123^{+0.00013}_{-0.00014}$
	Hartman et al. (2015)	0.1278 ± 0.0020	88.48 ± 0.57	$10.48^{+0.28}_{-0.40}$	4.2180278 ± 0.0000059	$2456194.12204 \pm 0.00040^a$
	Kokori et al. (2022)	–	–	–	4.2180226 ± 0.0000009	$2457868.67797 \pm 0.00024$
HAT-P−55b						
	This work	0.1220 ± 0.0007	86.80 ± 0.22	9.06 ± 0.16	$3.58523130^{+0.00000051}_{-0.00000051}$	$2458311.92255^{+0.00013}_{-0.00013}$
	Juncher et al. (2015)	0.1202 ± 0.0019	87.70 ± 0.56	9.79 ± 0.34	3.5852467 ± 0.0000064	$2456730.83468 \pm 0.00027^a$
	Ivshina & Winn (2022)	–	–	–	3.5852316 ± 0.0000010	$2458989.53140 \pm 0.00039$
	Kokori et al. (2022)	–	–	–	3.5852329 ± 0.0000012	2457720.3595 ± 0.0003
HAT-P−65b						
	This work	0.1006 ± 0.0009	88.3 ± 1.0	5.18 ± 0.07	$2.60544751^{+0.00000050}_{-0.00000049}$	$2458319.35067^{+0.00021}_{-0.00021}$
	Hartman et al. (2016)	0.1045 ± 0.0024	84.2 ± 1.3	4.57 ± 0.20	2.6054552 ± 0.0000031	$2456409.33263 \pm 0.00046^a$
	Chen et al. (2021b)	0.0994 ± 0.0025	$89.10^{+0.63}_{-0.83}$	$5.22^{+0.03}_{-0.04}$	–	–
	Kokori et al. (2022)	–	–	–	2.6054485 ± 0.0000009	2457149.2808 ± 0.0004

[a]Mid-transit times in BJD$_{\rm UTC}$.

The detrended MuSCAT2 light curves and best-fitting residuals are shown in Fig. 1.

In the second run, we attempted to evaluate the potential variation in transit depth as a function of wavelength. We fitted each light curve individually and fixed the values of i, $a/R_\star$, and $T_{\rm mid}$ to those obtained in the first run. The free parameters were $R_p/R_\star$, u_1, u_2, baseline function coefficients, and GP hyperparameters. For each passband, the weighted mean of $R_p/R_\star$ was taken as the final value and listed in Table 3.

3.2 TESS light curves

For the TESS light curves, we adopted the baseline function $b(\varphi)$ in the form of

$$b(\varphi) = c_0 + c_1 x + c_2 y, \tag{5}$$

where x and y are the coordinates of the target. The diluted transit model $\mu^*(t; \theta, f_c)$ was adopted to account for the potential dilution from nearby stars given the large pixel size of TESS. Therefore, $\mu^*(t; \theta, f_{\rm mid})b(\varphi)$ was adopted as the GP mean function for all the targets. For HAT-P-19b and HAT-P-51b, we used the supersampling feature of batman to account for the long cadence smearing effect (Kipping 2010). Since our purpose of modelling the TESS light curves was to measure the mid-transit times, we fixed the radius ratio $R_p/R_\star$, the inclination i, and the semimajor axis $a/R_\star$ to the values obtained from the analysis of the MuSCAT2 light curves. We also fixed the limb darkening coefficients to the pre-calculated values derived from the code of Espinoza & Jordán (2015). Each light curve had an independent mid-transit time. The detrended TESS light curves and their best-fitting residuals are shown in Fig. A1.

3.3 Transit parameter refinement

Based on MuSCAT2's light curve analysis of all nights and four passbands in the first run, we are able to refine the transit parameters for the four hot Jupiter systems, which are shown in Table 2 along with literature values for comparison.

For HAT-P-19b, HAT-P-51b, and HAT-P-55b, the transit parameters are derived from at least three MuSCAT2 transits, resulting in smaller uncertainties than those reported in the literature. In the case of HAT-P-65b, only two transits were observed by MuSCAT2, and only one of them covered the entire transit event. The uncertainties of i and $a/R_\star$ are slightly larger than those derived from two GTC transits (Chen et al. 2021b), but still consistent with the latter.

However, the transit parameters measured in different studies are not exactly in agreement. This discrepancy is likely due to the degeneracy between i and $a/R_\star$, since the measurements from different studies show a correlation trend (i.e. larger i with larger $a/R_\star$) consistent with the i-$a/R_\star$ degeneracy. Thanks to the multiple observations and the wide wavelength coverage of MuSCAT2, the transit parameters can be tightly constrained, with colour-dependent bias being eliminated.

3.4 Orbital period determination

We derived the mid-transit time of each transit for all the MuSCAT2 and TESS observations. To investigate the transit timing variations and to improve the orbital ephemeris, we also collected other mid-transit times published in the literature. All the mid-transit times have been converted to the BJD$_{\rm TDB}$ standard and presented in Table A3.

(i) For those with raw light curves available (Hartman et al. 2011, 2015, 2016; Chen et al. 2021b), we recalculated their mid-transit times using our light curve analysis method.

(ii) For HAT-P-19b, we did not include the mid-transit times in Baştürk et al. (2020), which have very small error bars and show a general downward offset from the linear ephemeris derived from the other times.

(iii) For HAT-P-51b, we discarded the mid-transit time of the 2018-11-23 transit because the computer time of that night was not properly synchronised with the Network Time Protocol server.

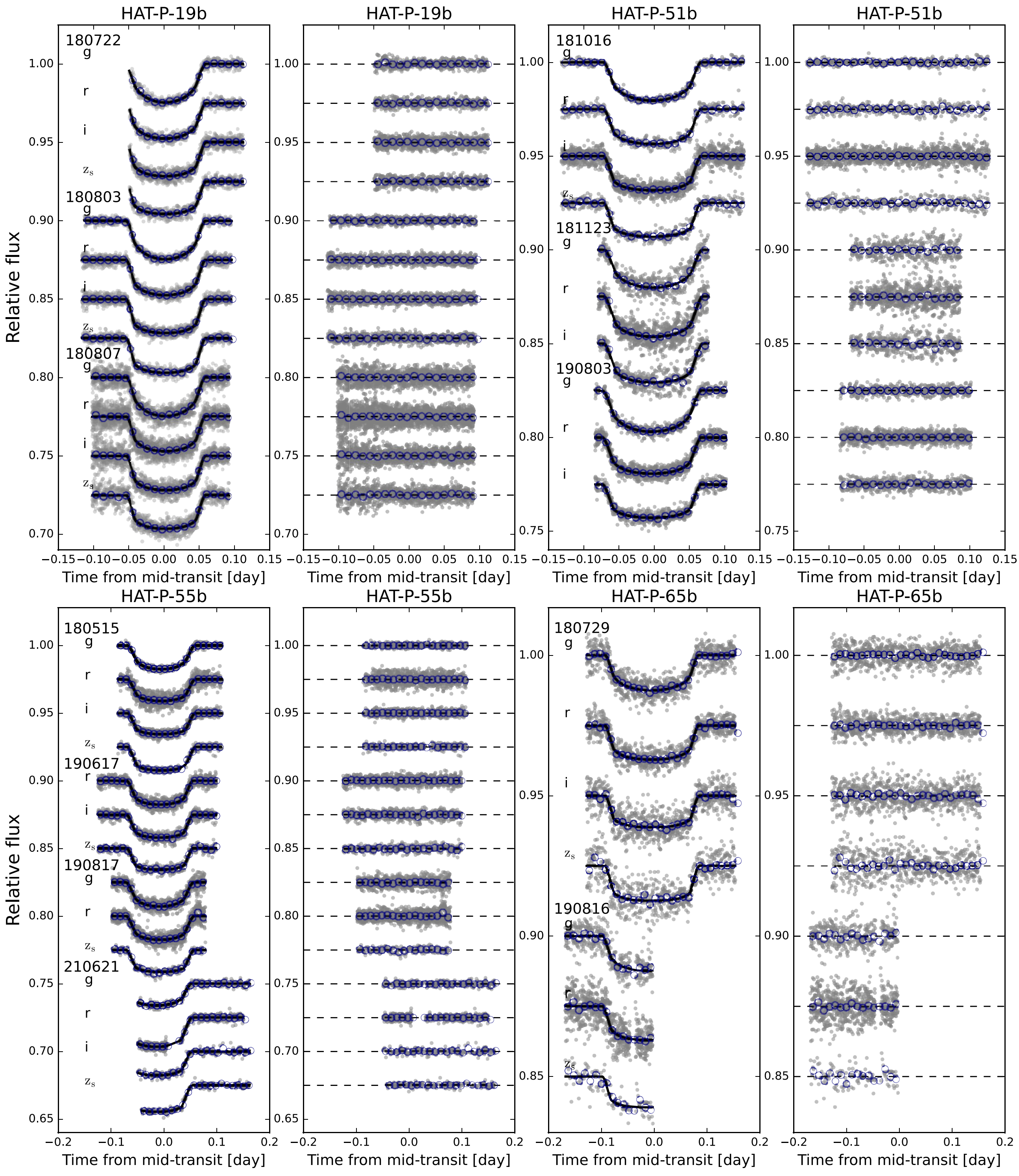

Figure 1. MuSCAT2 multicolour transit light curves of HAT-P-19b, HAT-P-51b, HAT-P-55b, and HAT-P-65b. The first and third panels show the light curves after removal of the systematics. The second and fourth panels show the best-fitting residuals. The black solid lines show the best-fitting model, and the navy circles show the 15-min binned points.

(iv) For HAT-P-55b and HAT-P-65b, we discarded the partial transits on 2021-06-21 and 2019-08-16, respectively.

The mid-transit times $T_{\rm mid}$ were fitted as a function of the epoch E using a linear model and a quadratic model, respectively. For the linear model, the planet was assumed to have a constant orbital period P:

$$T_{\rm mid} = T_0 + PE, \quad (6)$$

where T_0 is the mid-transit time at zero epoch. The zero epoch was optimised to give the smallest error bar for T_0. For the quadratic model, the planet was assumed to have a decaying orbital period:

$$T_{\rm mid} = T_0 + PE + \frac{1}{2}\frac{{\rm d}P}{{\rm d}E}E^2, \quad (7)$$

where dP/dE is the decay rate between successive transits. We used the Bayesian Information Criterion (BIC $= \chi^2 + k\log N$) to perform model comparison, where k is the number of free parameters and N is the number of data points.

The results of the model comparison are shown in Table 4. For the four planetary systems, the difference between the constant period model and the orbital decay model ΔBIC is -3.26, -2.64, -2.34, and -2.11, respectively. The constant period model is favoured with a lower BIC value in all four planetary systems, indicating that there is no evidence for orbital decay. Therefore, our results do not support the claims of potential orbital decay in HAT-P-19b (Hagey, Edwards & Boley 2022) and HAT-P-51b (Yeh, Jiang & A-thano 2023). Meanwhile, the timing residuals of the four systems with the best-fitting period model show no sign of transit timing variation (Fig. 2). The refined period and reference ephemeris are given in Table 2.

4 PHYSICAL PROPERTIES

Except for HAT-P-19, no follow-up physical property determinations have been made for these planetary systems. To refine their physical parameters, we used the IDL package EXOFASTV2 (Eastman et al. 2019) to perform a global modelling of the MuSCAT2 transit light curves, the RV measurements from the literature, the isochrones from the MESA Isochrones and Stellar Tracks (MIST; Dotter 2016), and the spectral energy distribution (SED) from broad-band photometry. The use of the MIST stellar evolutionary models produces consistent models for both isochrones and SED. The latest stellar parallax from the *Gaia* third data release (DR3; Gaia Collaboration 2022) provides an accurate prior on the stellar distance, which places a tight constraint on the stellar radius in the SED model. The collected broad-band photometry and *Gaia* DR3 stellar parallax are listed in Table A2.

We imposed Gaussian priors on the effective temperature $T_{\rm eff}$, the metallicity [Fe/H], the parallax from *Gaia* DR3, the quadratic LDCs, the transit period, and placed an upper limit of $3.1E(B-V)_{\rm S\&F}$[3] on A_V. We obtained priors of $T_{\rm eff}$ and [Fe/H] from Hartman et al. (2011), Hartman et al. (2015), Juncher et al. (2015), and Hartman et al. (2016) and adopted upper limits of $A_V < 0.27621$, 0.14849, 0.17019, and 0.27032 for HAT-P-19, HAT-P-51, HAT-P-55, and HAT-P-65, respectively. We ran the MCMC function of EXOFASTv2 to explore the posterior distributions of free parameters and adopted its default convergence criteria (Gelman-Rubin statistics $R_z < 1.01$ and independent draws $T_z > 1000$). The median and 1σ uncertainties of the derived physical parameters are listed in Table 5. The best-fitting SED models, RV models, and stellar evolutionary models are presented in Figs 3–5, respectively.

For HAT-P-19, we jointly fitted 12 MuSCAT2 light curves along with RV from Hartman et al. (2011). The physical parameters of the HAT-P-19 system have been recently updated by Baştürk et al. (2020). We derived consistent but marginally smaller values ($0.277^{+0.017}_{-0.016}$ $M_{\rm J}$, $1.008^{+0.014}_{-0.013}$ $R_{\rm J}$) for both planetary radius and mass than theirs ($0.284^{+0.017}_{-0.017}$ $M_{\rm J}$, $1.064^{+0.031}_{-0.034}$ $R_{\rm J}$).

For HAT-P-51, we jointly fitted 10 MuSCAT2 light curves along with RV from Hartman et al. (2015). Our derived planetary mass and radius ($0.307^{+0.021}_{-0.020}$ $M_{\rm J}$, $1.205^{+0.017}_{-0.016}$ $R_{\rm J}$) are both marginally smaller than those ($0.309^{+0.018}_{-0.018}$ $M_{\rm J}$, $1.293^{+0.054}_{-0.054}$ $R_{\rm J}$) in the discovery paper (Hartman et al. 2015).

For HAT-P-55, we jointly fitted 15 MuSCAT2 light curves along with RV from Juncher et al. (2015). We derived marginally larger mass and 2.4σ larger radius ($0.596^{+0.073}_{-0.072}$ $M_{\rm J}$, $1.324^{+0.023}_{-0.022}$ $R_{\rm J}$) for the planet, compared to those ($0.582^{+0.056}_{-0.056}$ $M_{\rm J}$, $1.182^{+0.055}_{-0.055}$ $R_{\rm J}$) in the discovery paper (Juncher et al. 2015). Our larger planetary radius is the result of both the larger radius ratio and the larger stellar radius ($1.105^{+0.018}_{-0.017}$ versus $1.011^{+0.036}_{-0.036}$ R$_\odot$).

For HAT-P-65, we jointly fitted 7 MuSCAT2 light curves, two GTC/OSIRIS light curves (Chen et al. 2021b), along with RV from Hartman et al. (2016). Our derived planetary mass and radius are marginally larger and 2.1σ smaller ($0.554^{+0.092}_{-0.091}$ $M_{\rm J}$, $1.611^{+0.024}_{-0.024}$ $R_{\rm J}$) than those in the discovery paper ($0.527^{+0.083}_{-0.083}$ $M_{\rm J}$, $1.89^{+0.13}_{-0.13}$ $R_{\rm J}$). Our smaller planetary radius is the result of both the smaller radius ratio and the smaller stellar radius ($1.666^{+0.024}_{-0.024}$ versus $1.860^{+0.096}_{-0.096}$ R$_\odot$). The difference in stellar radius comes from the transit-constrained stellar density, which could be biased by the degeneracy between i and $a/R_\star$, and was not constrained by the partial transits of Hartman et al. (2016).

5 VARIATION OF TRANSIT DEPTH WITH WAVELENGTH

Based on the MuSCAT2 data, we measured a difference between the maximum and minimum transit depths of 463 ± 293 ppm, 525 ± 424 ppm, 887 ± 370 ppm, and 1138 ± 758 ppm for HAT-P-19b, HAT-P-51b, HAT-P-55b, and HAT-P-65b, respectively, corresponding to 1.8 ± 1.1, 1.8 ± 1.5, 4.8 ± 2.0, and 5.4 ± 3.6 times the transit depth variation caused by one atmospheric scale height. The atmospheric scale height, $H = k_{\rm B}T_{\rm eq}/(\mu g_{\rm p})$, is estimated to be 0.0072, 0.0093, 0.0061, and 0.0107 $R_{\rm p}$, where $k_{\rm B}$ is the Boltzmann constant, $T_{\rm eq}$ is the planetary equilibrium temperature, $g_{\rm p}$ is the planetary surface gravity, and $\mu = 2.3$ g mol^{-1} is the mean molecular weight.

The transit depths measured by MuSCAT2 in the g, r, i, z_s bands sample a broad-band transmission spectrum for each planet. In particular, MuSCAT2's ability to perform simultaneous multicolour photometry eliminates the impact of stellar rotational modulation, allowing us to take a first look at the planetary atmospheres. The optical transmission spectrum is sensitive to both optical absorbers (such as alkali metals and metal oxides) and particle sizes of scattering sources. However, the broad-band averages the expected spectral features resulting from the planetary atmosphere, making it difficult to unambiguously distinguish the opacity sources of origin. Instead of using the broad-band transmission spectra to infer atmospheric properties, we tried to answer which targets have a higher priority for follow-up transmission spectroscopy.

Assuming that the variation in transit depth is potentially caused by the planetary atmosphere, we performed a simplified Bayesian spectral retrieval analysis on the MuSCAT2 broad-band transmission spectra. Two model hypotheses were considered, including a flat model and a planetary atmosphere model. The flat model has a constant planetary radius as the only free parameter. The planetary atmosphere model assumes a clear atmosphere of solar composition (C/O = 0.55, $\log Z/Z_\odot = 0$) in chemical equilibrium, consisting of two free parameters, the planetary radius at 10 mbar ($R_{\rm 10mbar}$) and the isothermal temperature ($T_{\rm iso}$). We used PETITRADTRANS (Mollière et al. 2019) to create the planetary atmosphere model, and PYMULTINEST (Buchner et al. 2014) to implement the multimodal

[3] https://irsa.ipac.caltech.edu/

Table 3. Chromatic radius ratios of four hot Jupiter systems.

Band (nm)	$R_p/R_\star$			
	HAT-P−19b	HAT-P−51b	HAT-P−55b	HAT-P−65b
g (400-550)	0.1352 ± 0.0009	0.1257 ± 0.0011	0.1224 ± 0.0011	0.0991 ± 0.0016
r (550-700)	0.1335 ± 0.0007	0.1260 ± 0.0010	0.1237 ± 0.0008	0.1010 ± 0.0013
i (700-820)	0.1343 ± 0.0007	0.1251 ± 0.0009	0.1214 ± 0.0010	0.0984 ± 0.0021
z_s (820-920)	0.1350 ± 0.0007	0.1239 ± 0.0014	0.1201 ± 0.0013	0.1041 ± 0.0031

Table 4. Comparison of the constant period model and the orbital decay model.

Parameter	Symbol	Constant period	Orbital decay
HAT-P−19b			
Number of data	n	27	27
Degrees of freedom	dof	24	23
Chi-square	χ^2	23.48	23.45
Reduce chi-square	χ^2/dof	0.98	1.02
Bayesian information criterion	BIC	33.37	36.63
RMS of residual (second)	RMS	80.8	81.1
HAT-P−51b			
Number of data	n	19	19
Degrees of freedom	dof	16	15
Chi-square statistic	χ^2	27.06	26.76
Reduce chi-square statistic	χ^2/dof	1.69	1.78
Bayesian information criterion	BIC	35.89	38.53
RMS of residual (second)	RMS	175.5	175.7
HAT-P−55b			
Number of data	n	30	30
Degrees of freedom	dof	27	26
Chi-square statistic	χ^2	19.46	18.40
Reduce chi-square statistic	χ^2/dof	0.72	0.71
Bayesian information criterion	BIC	29.66	32.00
RMS of residual (second)	RMS	107.2	106.3
HAT-P−65b			
Number of data	n	16	16
Degrees of freedom	dof	13	12
Chi-square statistic	χ^2	22.21	21.53
Reduce chi-square statistic	χ^2/dof	1.71	1.79
Bayesian information criterion	BIC	30.52	32.63
RMS of residual (second)	RMS	135.9	139.6

nested sampling (Feroz & Hobson 2008; Feroz, Hobson & Bridges 2009) for parameter estimation.

Fig.6 presents the MuSCAT2 broad-band transmission spectrum along with the retrieved atmosphere models. Compared to the flat model, the atmosphere model resulted in decreasing reduced chi-square values for HAT-P-19b (from 1.18 to 1.08), HAT-P-51b (from 0.58 to 0.10), and HAT-P-55b (from 2.25 to 0.24), but an increasing value for HAT-P-65b (from 1.08 to 1.70), indicating that the atmosphere model provides a better fit than the flat model for the first three planets. We also calculated the log-evidence to compare these two models, and obtained $\Delta \ln \mathcal{Z} (= \ln \mathcal{Z}_{\rm atmos} - \ln \mathcal{Z}_{\rm flat})$ values of -1.2 ± 0.1, -0.2 ± 0.1, 2.5 ± 0.1, and -0.5 ± 0.1 for HAT-P-19b, HAT-P-51b, HAT-P-55b, and HAT-P-65b, respectively. Therefore, HAT-P-55b is the only planet with moderate evidence in the Bayesian framework that a planetary atmosphere is required to explain the data, making it a priority target for future follow-up spectrophotometric observations.

Of the four planets, two have been observed for optical transmission spectra prior to our MuSCAT2 observations. Mallonn et al. (2015) obtained a flat featureless spectrum for HAT-P-19b using the R2500R grism of GTC's OSIRIS spectrograph, while Chen et al. (2021b) reported the detection of TiO and the possible detection of Na and VO in the atmosphere of HAT-P-65b using the R1000R grism of GTC OSIRIS. Therefore, we also performed retrievals on the combined MuSCAT2 and GTC data set for HAT-P-19b and HAT-P-65b. In this case, we adopted a more complicated planetary atmosphere model because more data points were available. The model assumes an isothermal atmosphere at a temperature of $T_{\rm iso}$ in chemical equilibrium controlled by the metallicity Z and the C/O ratio with a clear and a cloudy sector. The cloudy sector has a cloud fraction of ϕ, a cloud top at pressure $P_{\rm cloud}$, and a scattering amplitude $A_{\rm scatt}$ times that of H_2 Rayleigh scattering. To account for the offsets introduced by different orbital parameters in deriving the transit depth and different instrumental systematics, the GTC OSIRIS spectra were allowed to have a free offset in the retrieval.

Table 6 presents the retrieved parameters based on the combined MuSCAT2 and GTC data set for HAT-P-19b and HAT-P-65b. For HAT-P-19b, the atmospheric metallicity tends to be super solar. For HAT-P-65b, the retrieved parameters agree well with those of Chen et al. (2021b). Unfortunately, due to the lack of infrared wavelengths that cover sufficient molecular spectral features to characterize atmospheric chemistry and cloud altitude, it is difficult to constrain the parameters other than temperature, reference radius, and instrumental offset. Future transmission spectroscopy conducted with the *JWST*, together with the current optical transmission spectra, should be able to place more meaningful constraints on the atmospheric metallicity, cloud properties, and relative elemental ratios, paving the way for tracing planetary formation and migration histories (e.g. Öberg, Murray-Clay & Bergin 2011; Madhusudhan, Amin & Kennedy 2014; Mordasini et al. 2016; Lothringer et al. 2021; Ohno & Fortney 2023).

6 CONCLUSIONS

We performed simultaneous multicolour photometric observations of the transiting exoplanet systems HAT-P-19, HAT-P-51, HAT-P-55, and HAT-P-65 with the MuSCAT2 camera on the 1.52 m TCS telescope. We observed 12 transits for the four planets and obtained a total of 43 MuSCAT2 transit light curves. The transit parameters were revised based on the MuSCAT2 multicolour transit light curves. We also collected light curves for 56 transits from the TESS photometry, and combined the TESS timings with MuSCAT2 and literature timings to improve the orbital period and ephemeris estimates. We then consistently refined the physical parameters of these planetary systems by performing EXOFASTv2 global fits to the MuSCAT2 transit data, archival RV data, *Gaia* DR3 parallax, isochrones, and broad-band spectral energy distributions. Finally, we investigated the potential for atmospheric characterization using the MuSCAT2 multicolour transit depths for these four hot Jupiters. Our conclusions can be summarized as follows:

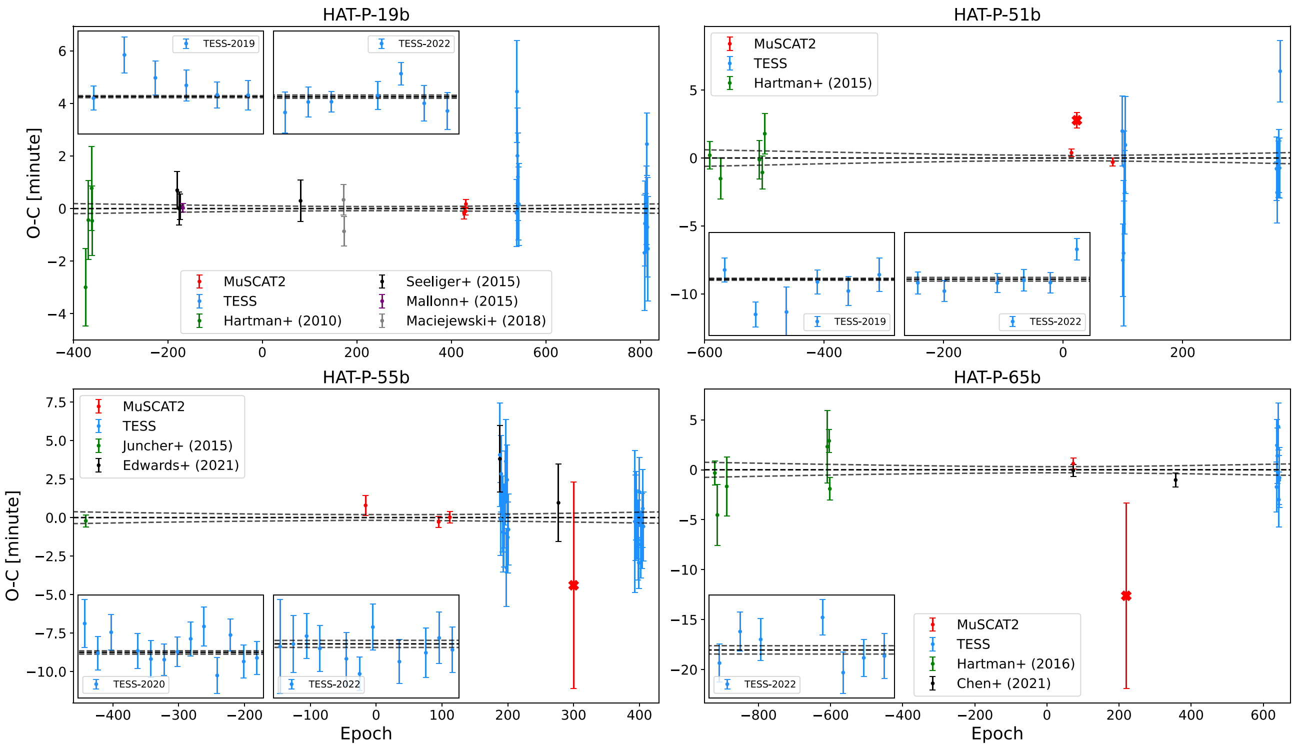

Figure 2. Timing residuals of four systems with the constant period model. Each data point is the difference between the observed mid-transit time and the best-fitting linear model. The middle dashed line is the zero line, the other two dashed lines show the range of 1σ uncertainty. The inset shows the zoomed view of the residuals of the TESS light curves. The crossed points were discarded in the period modelling.

Table 5. Stellar and planetary parameters derived from the EXOFASTv2 global fits.

Symbol	Parameter (Unit)	HAT-P−19	HAT-P−51	HAT-P−55	HAT-P−65
Stellar parameters					
$M_\star$	Mass ($M_\odot$)	$0.807^{+0.034}_{-0.030}$	$0.961^{+0.040}_{-0.036}$	$1.028^{+0.050}_{-0.048}$	$1.297^{+0.056}_{-0.053}$
$R_\star$	Radius ($R_\odot$)	$0.773^{+0.011}_{-0.010}$	$0.995^{+0.013}_{-0.013}$	$1.105^{+0.018}_{-0.017}$	$1.666^{+0.024}_{-0.024}$
$L_\star$	Luminosity ($L_\odot$)	$0.327^{+0.012}_{-0.013}$	$0.790^{+0.021}_{-0.022}$	$1.249^{+0.049}_{-0.045}$	$2.970^{+0.120}_{-0.120}$
$\rho_\star$	Density (cgs)	$2.468^{+0.018}_{-0.033}$	$1.380^{+0.012}_{-0.020}$	$1.073^{+0.036}_{-0.034}$	$0.397^{+0.003}_{-0.006}$
$\log g$	Surface gravity (cgs)	$4.5687^{+0.0066}_{-0.0067}$	$4.4256^{+0.0069}_{-0.0073}$	$4.3630^{+0.0140}_{-0.0130}$	$4.1079^{+0.0068}_{-0.0074}$
$T_{\rm eff}$	Effective temperature (K)	4962^{+39}_{-41}	5453^{+31}_{-32}	5804^{+37}_{-37}	5872^{+40}_{-40}
[Fe/H]	Metallicity (dex)	$0.166^{+0.070}_{-0.068}$	$0.302^{+0.052}_{-0.059}$	$0.003^{+0.049}_{-0.032}$	$0.208^{+0.050}_{-0.055}$
$[{\rm Fe/H}]_0$	Initial metallicity	$0.156^{+0.070}_{-0.068}$	$0.301^{+0.055}_{-0.059}$	$0.043^{+0.049}_{-0.041}$	$0.247^{+0.051}_{-0.051}$
Age	Age (Gyr)	$7.2^{+4.0}_{-4.0}$	$8.1^{+2.7}_{-2.5}$	$5.3^{+2.3}_{-1.9}$	$3.9^{+0.8}_{-0.8}$
A_V	*V*-band extinction (mag)	$0.228^{+0.035}_{-0.064}$	$0.119^{+0.021}_{-0.037}$	$0.074^{+0.049}_{-0.045}$	$0.180^{+0.049}_{-0.053}$
d	Distance (pc)	$201.8^{+0.6}_{-0.6}$	$445.0^{+3.2}_{-3.2}$	$525.4^{+2.8}_{-2.7}$	$750.0^{+12.0}_{-12.0}$
Planetary parameters:					
$R_{\rm p}$	Radius ($R_{\rm J}$)	$1.008^{+0.014}_{-0.013}$	$1.205^{+0.017}_{-0.016}$	$1.324^{+0.023}_{-0.022}$	$1.611^{+0.024}_{-0.024}$
$M_{\rm p}$	Mass ($M_{\rm J}$)	$0.277^{+0.017}_{-0.016}$	$0.307^{+0.021}_{-0.020}$	$0.596^{+0.073}_{-0.072}$	$0.554^{+0.092}_{-0.091}$
a	Semimajor axis (au)	$0.04599^{+0.00063}_{-0.00058}$	$0.05042^{+0.00068}_{-0.00065}$	$0.04628^{+0.00074}_{-0.00072}$	$0.04042^{+0.00057}_{-0.00055}$
$T_{\rm eq}$	Equilibrium temperature (K)	$981.2^{+7.7}_{-8.1}$	$1168.2^{+6.9}_{-7.0}$	$1367.0^{+11.0}_{-11.0}$	$1818.0^{+13.0}_{-13.0}$
K	RV semiamplitude (m s^{-1})	$40.9^{+2.2}_{-2.2}$	$39.7^{+2.4}_{-2.5}$	$77.6^{+9.1}_{-9.2}$	$68.0^{+11.0}_{-11.0}$
$\rho_{\rm p}$	Density (cgs)	$0.335^{+0.019}_{-0.019}$	$0.218^{+0.014}_{-0.014}$	$0.318^{+0.040}_{-0.039}$	$0.164^{+0.027}_{-0.027}$
$\log g_{\rm p}$	Surface gravity	$2.830^{+0.023}_{-0.024}$	$2.720^{+0.026}_{-0.028}$	$2.926^{+0.050}_{-0.056}$	$2.724^{+0.065}_{-0.077}$
Θ	Safronov number	$0.0313^{+0.0018}_{-0.0017}$	$0.0267^{+0.0017}_{-0.0017}$	$0.0405^{+0.0048}_{-0.0048}$	$0.0214^{+0.0035}_{-0.0035}$
$<F>$	Incident flux (10^9 erg s^{-1} cm^{-2})	$0.210^{+0.007}_{-0.007}$	$0.422^{+0.010}_{-0.010}$	$0.794^{+0.025}_{-0.024}$	$2.478^{+0.071}_{-0.069}$

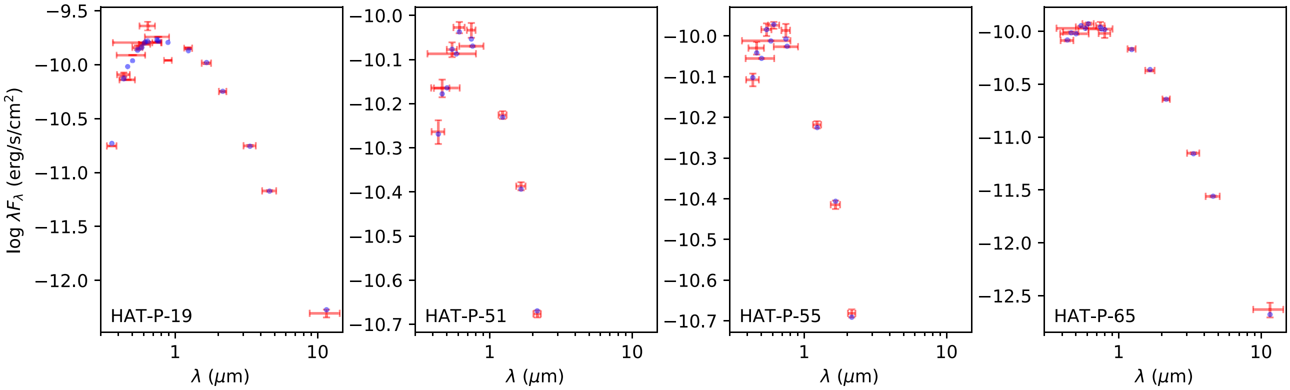

Figure 3. Spectral energy distributions (SEDs) of HAT-P-19, HAT-P-51, HAT-P-55, and HAT-P-65 from broad-band photometry. The red data points with error bars are the broad-band photometric measurements. The blue circles are the best-fitting SED model values.

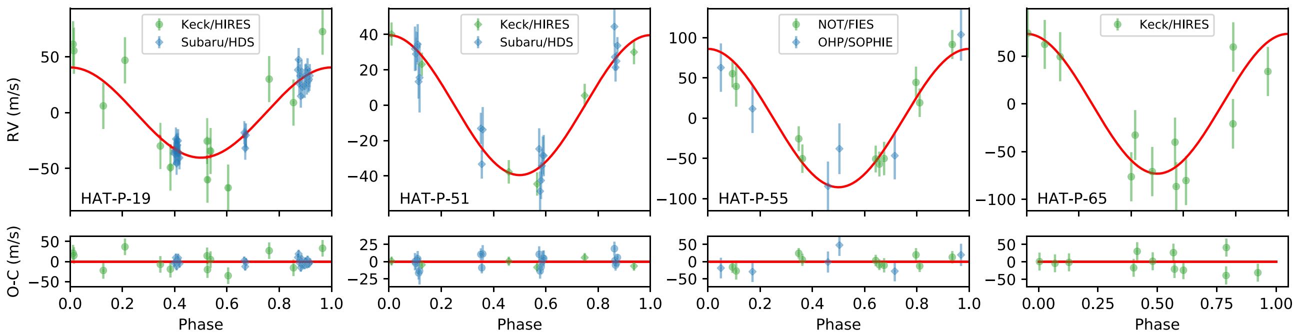

Figure 4. Radial velocity (RV) observations of HAT-P-19, HAT-P-51, HAT-P-55, and HAT-P-65. The red curves show the best-fitting model from the EXOFASTv2 fit.

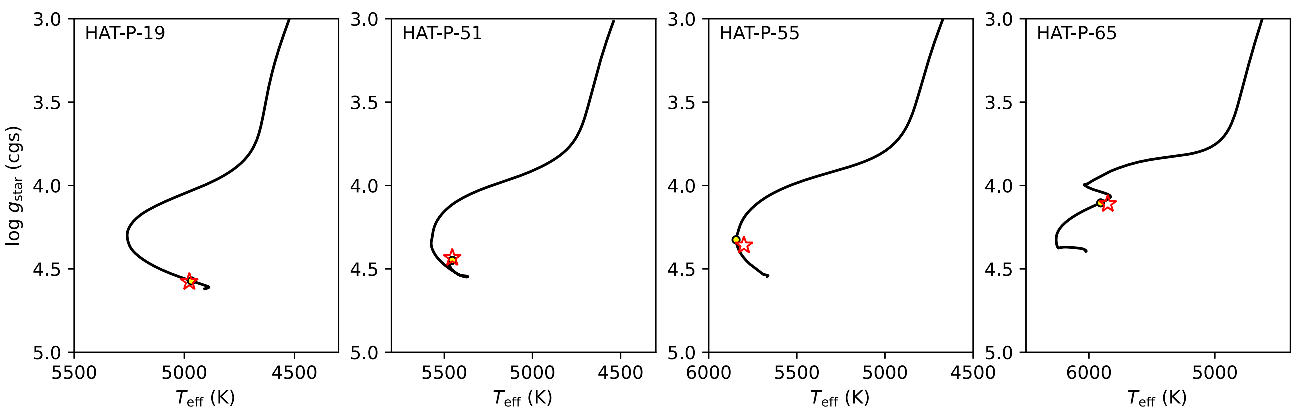

Figure 5. Stellar evolutionary tracks of HAT-P-19, HAT-P-51, HAT-P-55, and HAT-P-65. The black line is the MIST mass track interpolated with the best-fitting free parameters. The yellow circle highlights the mass track grid closest to the best-fitting Equivalent Evolutionary Phase (EEP) value. The red star indicates the best-fitting values of $T_{\rm eff}$ and $\log g_{\star}$.

– We have improved the transit parameter estimates for HAT-P-19b, HAT-P-51b, and HAT-P-55b, with smaller uncertainties than previous studies. The MuSCAT2 uncertainties for HAT-P-65b are slightly larger than those derived from the very precise GTC observations.

– We have consistently refined the physical parameters for all four planetary systems based on the improved transit parameters, which were derived from MuSCAT2 and GTC for HAT-P-65b, but only from MuSCAT2 for the other three. All the stellar and planetary radii are more tightly constrained than in previous studies, with typical relative errors of less than 2 per cent.

– We have improved the orbital period and ephemeris estimates for all four planetary systems. All of them are consistent with linear ephemeris. No significant transit timing variations or evidence of orbital decay were found. Based on our results, the typical uncertainties of the predicted mid-transit time by mid-2035 would

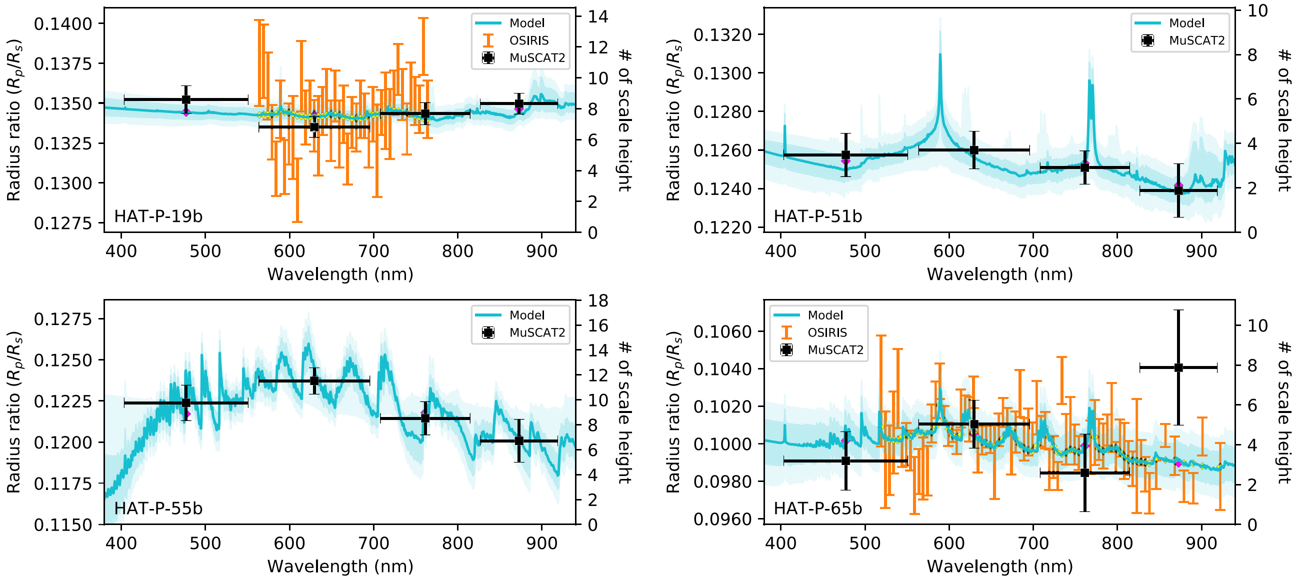

Figure 6. Broad-band transmission spectra of the four hot Jupiters (HAT-P-19b, HAT-P-51b, HAT-P-55b, and HAT-P-65b) along with the retrieved atmospheric models. For HAT-P-19b and HAT-P-65b, the retrievals were performed on the MuSCAT2 and OSIRIS combined dataset, with the assumption of patchy clouds and equilibrium chemistry. The OSIRIS data for HAT-P-19b and HAT-P-65b were obtained from Mallonn et al. (2015) and Chen et al. (2021b), respectively. For HAT-P-51b and HAT-P-55b, due to limited data points, the retrievals adopted a simplified assumption of cloud-free solar atmosphere.

Table 6. Parameter estimation for spectral retrievals.

Parameter	Prior	Posterior	
		HAT-P−19b	HAT-P−65b
$T_{\rm iso}$ (K)	$\mathcal{U}(500, 2500)$	681^{+118}_{-115}	1412^{+140}_{-43}
$R_{\rm 10mbar}$ ($R_{\rm J}$)	$\mathcal{U}(0.5, 2)$	$1.032^{+0.005}_{-0.008}$	$1.634^{+0.021}_{-0.024}$
$\log P_{\rm cloud}$ (bar)	$\mathcal{U}(-6, 2)$	$-2.3^{+2.8}_{-2.5}$	$-1.4^{+2.2}_{-2.8}$
$\log A_{\rm scatt}$	$\mathcal{U}(0, 4)$	$1.7^{+1.4}_{-1.2}$	$2.1^{+1.3}_{-1.3}$
C/O	$\mathcal{U}(0.1, 1.6)$	$0.76^{+0.55}_{-0.45}$	$0.94^{+0.38}_{-0.46}$
$\log Z/Z_{\odot}$	$\mathcal{U}(-2, 3)$	$1.8^{+0.8}_{-1.1}$	$0.3^{+1.4}_{-1.4}$
ϕ	$\mathcal{U}(0, 1)$	$0.38^{+0.37}_{-0.25}$	$0.40^{+0.27}_{-0.24}$
Offset (ppm)	$\mathcal{U}(-5000, 5000)$	1299^{+115}_{-118}	-54^{+159}_{-164}

be 33, 84, 77, and 104 s for HAT-P-19b, HAT-P-51b, HAT-P-55b, and HAT-P-65b, respectively, which are reasonably precise even in the ARIEL era.

– We have found that planetary atmosphere models can improve the fit to the MuSCAT2 broad-band transmission spectra of HAT-P-19b, HAT-P-51b, and HAT-P-55b compared to a flat line based on χ^2 statistics. However, in terms of Bayesian model statistical significance, only HAT-P-55b shows (moderate) evidence of the presence of a planetary atmosphere. This makes HAT-P-55b a priority target for future transmission spectroscopy.

ACKNOWLEDGEMENTS

GC acknowledges the support by the B-type Strategic Priority Program of the Chinese Academy of Sciences (grant no. XDB41000000), the National Natural Science Foundation of China (NSFC; grant nos. 42075122, 12122308), Youth Innovation Promotion Association CAS (2021315), and the Minor Planet Foundation of the Purple Mountain Observatory. YM acknowledges the support by NSFC (grant no. 12033010). MT is supported by JSPS KAKENHI grant no. 18H05442. E.E-B. acknowledges financial support from the European Union and the State Agency of Investigation of the Spanish Ministry of Science and Innovation (MICINN) under the grant PRE2020-093107 of the Pre-Doc Program for the Training of Doctors (FPI-SO) through FSE funds. RL acknowledges funding from University of La Laguna through the Margarita Salas Fellowship from the Spanish Ministry of Universities ref. UNI/551/2021-May 26, and under the EU Next Generation funds. MS acknowledges the support of the Italian National Institute of Astrophysics (INAF) through the project 'The HOT-ATMOS Project: characterizing the atmospheres of hot giant planets as a key to understand the exoplanet diversity' (1.05.01.85.04). This work is partly supported by JSPS KAKENHI grant numbers JP18H05439, JP21K13955, JP21K20376, and JST CREST grant number JPMJCR1761. This article is based on observations made with the MuSCAT2 instrument, developed by ABC, at Telescopio Carlos Sánchez operated on the island of Tenerife by the IAC in the Spanish Observatorio del Teide. This paper includes data collected with the TESS mission, obtained from the MAST data archive at the Space Telescope Science Institute (STScI). Funding for the TESS mission is provided by the NASA Explorer Program. STScI is operated by the Association of Universities for Research in Astronomy, Inc., under NASA contract NAS 5–26555. This work has made use of data from the European Space Agency (ESA) mission *Gaia* (https://www.cosmos.esa.int/gaia), processed by the *Gaia* Data Processing and Analysis Consortium (DPAC; https://www.cosmos.esa.int/web/gaia/dpac/consortium). Funding for the DPAC has been provided by national institutions, in particular, the institutions participating in the *Gaia* Multilateral Agreement. This work has made use of MATPLOTLIB (Hunter 2007), the VizieR catalogue access tool, CDS, Strasbourg, France (Ochsenbein, Bauer & Marcout 2000), and TEPCat (Southworth 2011).

DATA AVAILABILITY

The data underlying this article will be shared at reasonable request to the corresponding author. The reduced light curves presented in this work will be made available at the CDS (http://cdsarc.u-strasbg.fr/).

REFERENCES

Baştürk Ö., Yalçınkaya S., Esmer E. M., Tanrıverdi T., Mancini L., Daylan T., Southworth J., Keten B., 2020, MNRAS, 496, 4174
Buchner J. et al., 2014, A&A, 564, A125
Charbonneau D., Brown T. M., Noyes R. W., Gilliland R. L., 2002, ApJ, 568, 377
Chen G. et al., 2014, A&A, 563, A40
Chen G. et al., 2021a, MNRAS, 500, 5420
Chen G., Pallé E., Parviainen H., Murgas F., Yan F., 2021b, ApJ, 913, L16
Cutri R. M. et al., 2014, VizieR Online Data Catalog, II/328
Dotter A., 2016, ApJS, 222, 8
Droege T. F., Richmond M. W., Sallman M. P., Creager R. P., 2006, PASP, 118, 1666
Eastman J., Siverd R., Gaudi B. S., 2010, PASP, 122, 935
Eastman J. D. et al., 2019, preprint (arXiv:1907.09480)
Edwards B. et al., 2021, MNRAS, 504, 5671
Espinoza N., Jordán A., 2015, MNRAS, 450, 1879
Feroz F., Hobson M. P., 2008, MNRAS, 384, 449
Feroz F., Hobson M. P., Bridges M., 2009, MNRAS, 398, 1601
Foreman-Mackey D. et al., 2013, Astrophysics Source Code Library, recordascl:1303.002
Foreman-Mackey D., Agol E., Ambikasaran S., Angus R., 2017, AJ, 154, 220
Fortney J. J., Marley M. S., Barnes J. W., 2007, ApJ, 659, 1661
Gaia Collaboration, 2022, VizieR Online Data Catalog, I/355
Gibson N. P., Aigrain S., Roberts S., Evans T. M., Osborne M., Pont F., 2012, MNRAS, 419, 2683
Greiner J. et al., 2008, PASP, 120, 405
Hagey S. R., Edwards B., Boley A. C., 2022, AJ, 164, 220
Hartman J. D. et al., 2011, ApJ, 726, 52
Hartman J. D. et al., 2015, AJ, 150, 168
Hartman J. D. et al., 2016, AJ, 152, 182
Henden A. A., Templeton M., Terrell D., Smith T. C., Levine S., Welch D., 2016, VizieR Online Data Catalog, II/336
Hunter J. D., 2007, Comput. Sci. Eng., 9, 90
Ivshina E. S., Winn J. N., 2022, ApJS, 259, 62
Jenkins J. M. et al., 2016, in Chiozzi G., Guzman J. C., eds, Proc. SPIE Conf. Ser.Vol. 9913, Software and Cyberinfrastructure for Astronomy IV. SPIE, Bellingham, p. 99133E
Juncher D. et al., 2015, PASP, 127, 851
Kipping D. M., 2010, MNRAS, 408, 1758
Kokori A. et al., 2022, ApJS, 258, 40
Kreidberg L., 2015, Astrophysics Source Code Library, recordascl:1510.002
Lightkurve Collaboration, 2018, Lightkurve: Kepler and TESS Time Series Analysis in Python, preprint(ascl:1812.013)
Lothringer J. D., Rustamkulov Z., Sing D. K., Gibson N. P., Wilson J., Schlaufman K. C., 2021, ApJ, 914, 12
Luque R. et al., 2020, A&A, 642, A50
Maciejewski G., Stangret M., Ohlert J., Basaran C. S., Maciejczak J., Puciata-Mroczynska M., Boulanger E., 2018, Inf. Bull. Var. Stars, 6243, 1
Madhusudhan N., Amin M. A., Kennedy G. M., 2014, ApJ, 794, L12
Madhusudhan N., Agúndez M., Moses J. I., Hu Y., 2016, Space Sci. Rev., 205, 285
Mallonn M. et al., 2015, A&A, 580, A60
Mancini L. et al., 2014, MNRAS, 443, 2391
Mandel K., Agol E., 2002, ApJ, 580, L171
Mayor M., Queloz D., 1995, Nature, 378, 355
Medan I., Lepine S., Hartman Z., 2021, AJ, 161 234
Mollière P., Wardenier J. P., van Boekel R., Henning T., Molaverdikhani K., Snellen I. A. G., 2019, A&A, 627, A67
Mordasini C., van Boekel R., Mollière P., Henning T., Benneke B., 2016, ApJ, 832, 41
Narita N. et al., 2015, J. Astron. Telesc. Instrum. Syst., 1, 045001
Narita N. et al., 2019, J. Astron. Telesc. Instrum. Syst., 5, 015001
Narita N. et al., 2020, in Proc. SPIE Conf. Ser. Vol. SPIE, Bellingham, p. 114475K
Öberg K. I., Murray-Clay R., Bergin E. A., 2011, ApJ, 743, L16
Ochsenbein F., Bauer P., Marcout J., 2000, A&AS, 143, 23
Ohno K., Fortney J. J., 2023, ApJ, 946, 18
Parviainen H. et al., 2019, A&A, 630, A89
Ricker G. R. et al., 2015, J. Astron. Telesc. Instrum. Syst., 1, 014003
Seager S., Mallén-Ornelas G., 2003, ApJ, 585, 1038
Seager S., Sasselov D. D., 2000, ApJ, 537, 916
Seeliger M. et al., 2015, MNRAS, 451, 4060
Southworth J., 2011, MNRAS, 417, 2166
Yeh L.-C., Jiang I.-G., A-thano N., 2024, New Astronomy, 106, 102130
Zacharias N., Finch C., Frouard J., 2017, VizieR Online Data Catalog, I/340

APPENDIX A: ADDITIONAL TABLES AND FIGURES

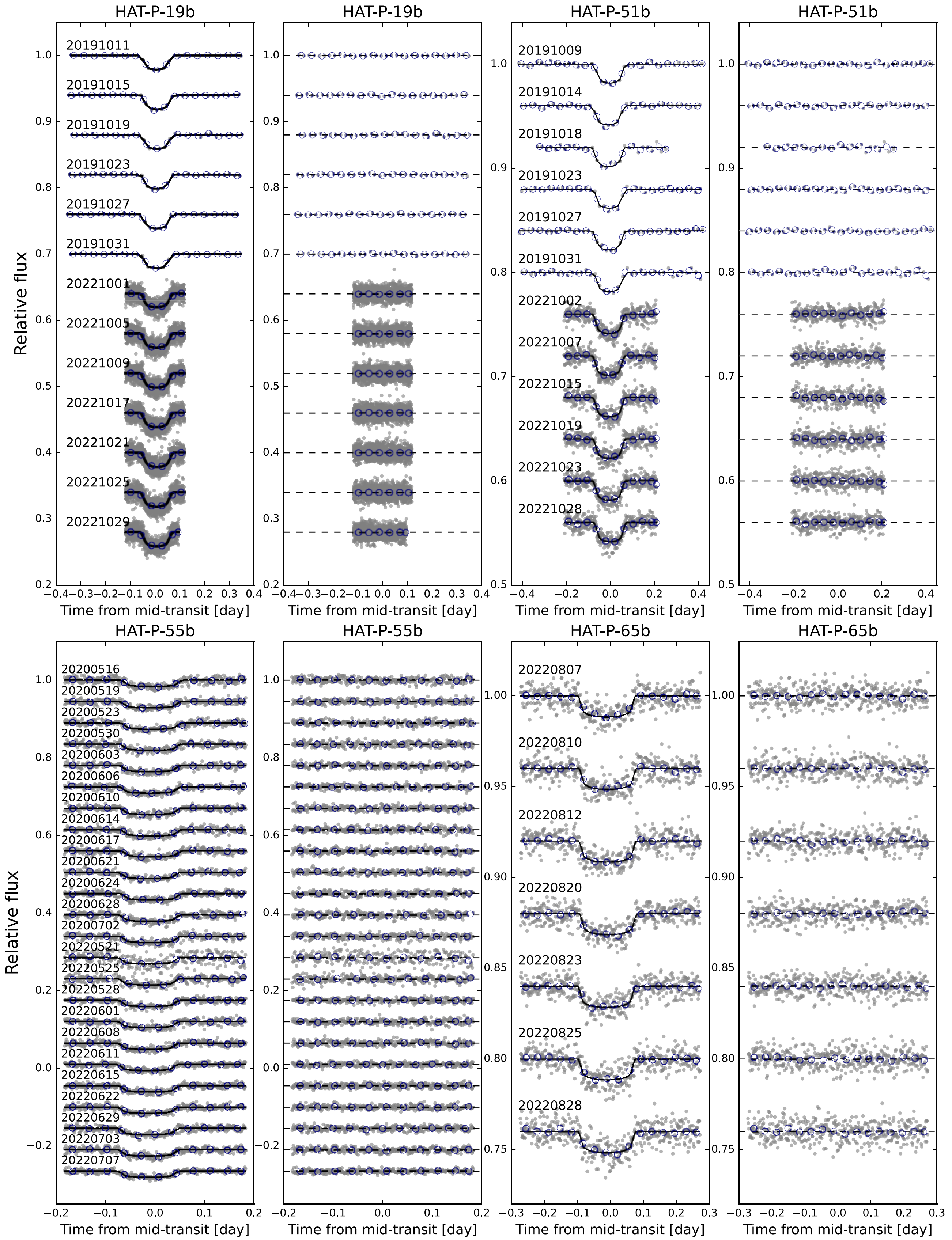

Figure A1. TESS transit light curves of HAT-P-19b, HAT-P-51b, HAT-P-55b, and HAT-P-65b. The first and third panels show the light curves after removal of systematics and the solid lines show the best-fitting model, the second and fourth panels show the best-fitting residual, and the navy circles show the 60-min binned points.

Table A1. Adopted priors for LDCs.

System	Band	u_1	u_2
HAT-P−19	g	$\mathcal{N}(0.8106, 0.0743)$	$\mathcal{N}(0.0221, 0.0659)$
HAT-P−19	r	$\mathcal{N}(0.5636, 0.0560)$	$\mathcal{N}(0.1680, 0.0410)$
HAT-P−19	i	$\mathcal{N}(0.4446, 0.0408)$	$\mathcal{N}(0.1993, 0.0263)$
HAT-P−19	z_s	$\mathcal{N}(0.3714, 0.0342)$	$\mathcal{N}(0.2144, 0.0202)$
HAT-P−51	g	$\mathcal{N}(0.6814, 0.0672)$	$\mathcal{N}(0.1280, 0.0538)$
HAT-P−51	r	$\mathcal{N}(0.4614, 0.0533)$	$\mathcal{N}(0.2385, 0.0346)$
HAT-P−51	i	$\mathcal{N}(0.3665, 0.0419)$	$\mathcal{N}(0.2506, 0.0255)$
HAT-P−51	z_s	$\mathcal{N}(0.3051, 0.0351)$	$\mathcal{N}(0.2546, 0.0192)$
HAT-P−55	g	$\mathcal{N}(0.5792, 0.0640)$	$\mathcal{N}(0.2048, 0.0472)$
HAT-P−55	r	$\mathcal{N}(0.3883, 0.0479)$	$\mathcal{N}(0.2781, 0.0277)$
HAT-P−55	i	$\mathcal{N}(0.3104, 0.0390)$	$\mathcal{N}(0.2745, 0.0206)$
HAT-P−55	z_s	$\mathcal{N}(0.2602, 0.0345)$	$\mathcal{N}(0.2725, 0.0171)$
HAT-P−65	g	$\mathcal{N}(0.5898, 0.0630)$	$\mathcal{N}(0.1966, 0.0464)$
HAT-P−65	r	$\mathcal{N}(0.3886, 0.0496)$	$\mathcal{N}(0.2800, 0.0292)$
HAT-P−65	i	$\mathcal{N}(0.3064, 0.0414)$	$\mathcal{N}(0.2807, 0.0225)$
HAT-P−65	z_s	$\mathcal{N}(0.2548, 0.0358)$	$\mathcal{N}(0.2774, 0.0182)$

Table A2. Broad-band photometry and stellar parallax of HAT-P−19, HAT-P−51, HAT-P−55, and HAT-P−65.

Passband	HAT-P−19 (mag)	Ref.	HAT-P−51 (mag)	Ref.	HAT-P−55 (mag)	Ref.	HAT-P−65 (mag)	Ref.
Johnson B	13.834 ± 0.051	1	14.261 ± 0.067	1	13.871 ± 0.039	1	13.818 ± 0.021	1
Johnson V	12.853 ± 0.055	1	13.440 ± 0.042	1	13.207 ± 0.039	1	13.145 ± 0.029	1
Johnson R	11.990 ± 0.100	2	–	–	–	–	–	–
Johnson I	–	–	–	–	–	–	12.456 ± 0.101	6
SDSS u'	15.589 ± 0.005	3	–	–	–	–	–	–
SDSS g'	13.779 ± 0.003	3	13.839 ± 0.050	1	13.501 ± 0.039	1	13.445 ± 0.016	3
SDSS r'	12.659 ± 0.002	3	13.194 ± 0.032	1	13.060 ± 0.021	1	12.948 ± 0.033	3
SDSS i'	12.406 ± 0.001	3	12.998 ± 0.042	1	12.880 ± 0.041	1	12.784 ± 0.097	3
SDSS z'	12.623 ± 0.004	3	–	–	–	–	–	–
2MASS J	11.095 ± 0.020	3	12.039 ± 0.022	5	12.020 ± 0.022	5	11.892 ± 0.026	5
2MASS H	10.644 ± 0.022	3	11.645 ± 0.023	5	11.714 ± 0.026	5	11.604 ± 0.022	5
2MASS K_s	10.546 ± 0.019	3	11.614 ± 0.020	5	11.627 ± 0.025	5	11.528 ± 0.025	5
*WISE*1	10.495 ± 0.022	3	–	–	–	–	11.494 ± 0.023	5
*WISE*2	10.557 ± 0.020	3	–	–	–	–	11.532 ± 0.021	5
*WISE*3	10.561 ± 0.091	3	–	–	–	–	11.373 ± 0.172	5
Gaia	12.546 ± 0.003	4	13.271 ± 0.003	4	13.083 ± 0.003	4	12.981 ± 0.003	4
Gaia BP	13.059 ± 0.003	4	13.686 ± 0.003	4	13.414 ± 0.003	4	13.332 ± 0.003	4
Gaia RP	11.884 ± 0.004	4	12.698 ± 0.004	4	12.590 ± 0.004	4	12.468 ± 0.004	4
Parallax (mas)	4.96 ± 0.01	4	2.25 ± 0.02	4	1.90 ± 0.01	4	1.32 ± 0.03	4

References: (1) Henden et al. (2015); (2) Zacharias, Finch & Frouard (2017); (3) Medan, Lepine & Hartman (2022); (4) Gaia Collaboration (2022); (5) Cutri & et al. (2014); (6) Droege et al. (2006).

Table A3. Mid-transit times of the four hot Jupiters.

Planet	Telescope	$T_{mid} - 2450000[BJD_{TDB}]$	Ref.
HAT-P−19b	TCS	8322.61426 ± 0.00016	1
HAT-P−19b	TCS	8334.64066 ± 0.00010	1
HAT-P−19b	TCS	8338.64963 ± 0.00012	1
HAT-P−19b	TESS	8767.58920 ± 0.00089	1
HAT-P−19b	TESS	8771.60119 ± 0.00135	1
HAT-P−19b	TESS	8775.60828 ± 0.00126	1
HAT-P−19b	TESS	8779.61650 ± 0.00115	1
HAT-P−19b	TESS	8783.62458 ± 0.00097	1
HAT-P−19b	TESS	8787.63334 ± 0.00109	1
HAT-P−19b	TESS	9853.96840 ± 0.00153	1
HAT-P−19b	TESS	9857.97795 ± 0.00112	1
HAT-P−19b	TESS	9861.98675 ± 0.00077	1
HAT-P−19b	TESS	9870.00479 ± 0.00103	1
HAT-P−19b	TESS	9874.01519 ± 0.00082	1
HAT-P−19b	TESS	9878.02177 ± 0.00132	1
HAT-P−19b	TESS	9882.02999 ± 0.00138	1
HAT-P−19b	FLWO 1.2 m	5111.57694 ± 0.00102	2[a]
HAT-P−19b	FLWO 1.2 m	5135.63142 ± 0.00104	2[a]
HAT-P−19b	FLWO 1.2 m	5163.69374 ± 0.00111	2[a]
HAT-P−19b	FLWO 1.2 m	5167.70166 ± 0.00092	2[a]
HAT-P−19b	Jena 0.6 m	5889.28345 ± 0.00049	3
HAT-P−19b	Jena 0.6 m	5905.31810 ± 0.00044	3
HAT-P−19b	CA-DLR 1.2 m	5913.33571 ± 0.00034	3
HAT-P−19b	Jena 0.6 m	6935.57559 ± 0.00055	3
HAT-P−19b	GTC	5937.38839 ± 0.00011	4
HAT-P−19b	Toruń 0.6 m	7300.37489 ± 0.00040	5
HAT-P−19b	Toruń 0.6 m	7304.38284 ± 0.00039	5
HAT-P−51b	TCS	8408.58379 ± 0.00019	1
HAT-P−51b	TCS	8446.55780 ± 0.00040	1
HAT-P−51b	TCS	8699.62675 ± 0.00021	1
HAT-P−51b	TESS	8767.11668 ± 0.00179	1
HAT-P−51b	TESS	8771.32811 ± 0.00186	1
HAT-P−51b	TESS	8775.54648 ± 0.00372	1
HAT-P−51b	TESS	8779.76896 ± 0.00179	1
HAT-P−51b	TESS	8783.98563 ± 0.00212	1
HAT-P−51b	TESS	8788.20607 ± 0.00247	1
HAT-P−51b	TESS	9855.36415 ± 0.00161	1
HAT-P−51b	TESS	9859.58096 ± 0.00155	1
HAT-P−51b	TESS	9868.01820 ± 0.00144	1
HAT-P−51b	TESS	9872.23663 ± 0.00162	1
HAT-P−51b	TESS	9876.45429 ± 0.00153	1
HAT-P−51b	TESS	9880.67726 ± 0.00157	1
HAT-P−51b	FLWO 1.2 m	5856.68101 ± 0.00071	6[a]
HAT-P−51b	FLWO 1.2 m	5932.60419 ± 0.00105	6[a]
HAT-P−51b	FLWO 1.2 m	6206.77652 ± 0.00098	6[a]
HAT-P−51b	FLWO 1.2 m	6227.86597 ± 0.00084	6[a]
HAT-P−51b	FLWO 1.2 m	6244.74004 ± 0.00103	6[a]
HAT-P−55b	TCS	8254.55943 ± 0.00046	1
HAT-P−55b	TCS	8652.51935 ± 0.00024	1
HAT-P−55b	TCS	8713.46849 ± 0.00025	1
HAT-P−55b	TCS	9387.48890 ± 0.00466	1
HAT-P−55b	TESS	8985.94888 ± 0.00233	1
HAT-P−55b	TESS	8989.53122 ± 0.00165	1
HAT-P−55b	TESS	8993.11849 ± 0.00172	1
HAT-P−55b	TESS	9000.28713 ± 0.00171	1
HAT-P−55b	TESS	9003.87156 ± 0.00181	1
HAT-P−55b	TESS	9007.45673 ± 0.00153	1
HAT-P−55b	TESS	9011.04274 ± 0.00144	1
HAT-P−55b	TESS	9014.62923 ± 0.00167	1
HAT-P−55b	TESS	9018.21567 ± 0.00189	1
HAT-P−55b	TESS	9021.79611 ± 0.00175	1
HAT-P−55b	TESS	9025.38530 ± 0.00158	1
HAT-P−55b	TESS	9028.96794 ± 0.00160	1
HAT-P−55b	TESS	9032.55352 ± 0.00160	1
HAT-P−55b	TESS	9720.91828 ± 0.00319	1
HAT-P−55b	TESS	9724.50368 ± 0.00194	1
HAT-P−55b	TESS	9728.08945 ± 0.00154	1
HAT-P−55b	TESS	9731.67384 ± 0.00156	1
HAT-P−55b	TESS	9738.84360 ± 0.00180	1
HAT-P−55b	TESS	9742.42780 ± 0.00115	1
HAT-P−55b	TESS	9746.01622 ± 0.00156	1
HAT-P−55b	TESS	9753.18433 ± 0.00150	1
HAT-P−55b	TESS	9760.35539 ± 0.00168	1
HAT-P−55b	TESS	9763.94164 ± 0.00175	1
HAT-P−55b	TESS	9767.52606 ± 0.00155	1
HAT-P−55b	FLWO 1.2 m	6730.83546 ± 0.00027	7
HAT-P−55b	Haleadkala	8985.9487 ± 0.0015	8
HAT-P−55b	Haleadkala	9305.0323 ± 0.0018	8
HAT-P−65b	TCS	8329.54876 ± 0.00038	1
HAT-P−65b	TCS	8712.54036 ± 0.00645	1
HAT-P−65b	TESS	9799.01953 ± 0.00174	1
HAT-P−65b	TESS	9801.62787 ± 0.00181	1
HAT-P−65b	TESS	9804.23259 ± 0.00192	1
HAT-P−65b	TESS	9812.05096 ± 0.00164	1
HAT-P−65b	TESS	9814.65134 ± 0.00191	1
HAT-P−65b	TESS	9817.25814 ± 0.00170	1
HAT-P−65b	TESS	9819.86376 ± 0.00209	1
HAT-P−65b	FLWO 1.2 m	5739.73328 ± 0.00083	9[a]
HAT-P−65b	FLWO 1.2 m	5757.96850 ± 0.00212	9[a]
HAT-P−65b	FLWO 1.2 m	5825.71212 ± 0.00205	9[a]
HAT-P−65b	FLWO 1.2 m	6552.63474 ± 0.00253	9[a]
HAT-P−65b	FLWO 1.2 m	6565.66238 ± 0.00079	9[a]
HAT-P−65b	FLWO 1.2 m	6570.86994 ± 0.00077	9[a]
HAT-P−65b	GTC	8329.54829 ± 0.00041	10[a]
HAT-P−65b	GTC	9069.49471 ± 0.00048	10[a]

[a]These mid-transit times have been recalculated using our light-curve analysis method.

References: (1) This work; (2) Hartman et al. (2011); (3) Seeliger et al. (2015); (4) Mallonn et al. (2015); (5) Maciejewski et al. (2018); (6) Hartman et al. (2015); (7) Juncher et al. (2015); (8) Edwards et al. (2021); (9) Hartman et al. (2016); (10) Chen et al. (2021b).

[1] *CAS Key Laboratory of planetary sciences, Purple Mountain Observatory, Chinese Academy of Sciences, Nanjing 210023, China*
[2] *School of Astronomy and Space Science, University of Science and Technology of China, Hefei 230026, China*
[3] *CAS Center for Excellence in Comparative Planetology, Hefei 230026, China*
[4] *Instituto de Astrofísica de Canarias, Vía Láctea s/n, E-38205 La Laguna, Tenerife, Spain*
[5] *Departamento de Astrofísica, Universidad de La Laguna, C/ Padre Herrera, E-38206 La Laguna, Spain*
[6] *Department of Multi-Disciplinary Sciences, Graduate School of Arts and Sciences, The University of Tokyo, 3-8-1 Komaba, Meguro, Tokyo 153-8902, Japan*
[7] *Komaba Institute for Science, The University of Tokyo, 3-8-1 Komaba, Meguro, Tokyo 153-8902, Japan*
[8] *Okayama Observatory, Kyoto University, 3037-5 Honjo, Kamogatacho, Asakuchi, Okayama 719-0232, Japan*
[9] *Department of Physical Sciences, Ritsumeikan University, Kusatsu, Shiga 525-8577, Japan*
[10] *Lund Observatory, Division of Astrophysics, Department of Physics, Lund University, Box 43, 22100 Lund, Sweden*
[11] *Astrobiology Center, 2-21-1 Osawa, Mitaka, Tokyo 181-8588, Japan*
[12] *National Astronomical Observatory of Japan, 2-21-1 Osawa, Mitaka, Tokyo 181-8588, Japan*
[13] *Astronomical Science Program, Graduate University for Advanced Studies, SOKENDAI, 2-21-1, Osawa, Mitaka, Tokyo 181-8588, Japan*
[14] *Department of Astronomy & Astrophysics, University of Chicago, Chicago, IL 60637, USA*
[15] *School of Architecture, Universidad Europea de Canarias, C/ Inocencio Garcia 1, E-38300, La Orotava, Tenerife, Spain*
[16] *INAF - Osservatorio Astronomico di Padova, Vicolo dell'Osservatorio 5, I-35122 Padova, Italy*
[17] *Department of Astronomy, University of Tokyo, 7-3-1 Hongo, Bunkyo-ku, Tokyo 113-0033, Japan*

This paper has been typeset from a TEX/LATEX file prepared by the author.